The 1999 Hector Mine Earthquake, Southern California: Vector Near-Field Displacements from ERS InSAR

David T. Sandwell, Lydie Sichoix, and Bridget Smith

Scripps Institution of Oceanography
La Jolla CA 92093-0225

Ph. 858 534-7109
e-mail: dsandwell@ucsd.edu

submitted to: BSSA, Special Section on the Hector Mine Earthquake, October 16, 2000; in press. August 2001

Abstract

Two components of fault slip are uniquely determined from two line-of-sight (LOS) radar interferograms by assuming that the fault-normal component of displacement is zero. We use this approach with ascending and descending interferograms from the ERS satellites to estimate surface slip along the Hector Mine earthquake rupture. The LOS displacement is determined by visually counting fringes to within 1 km of the outboard ruptures. These LOS estimates and uncertainties are then transformed into strike- and dip-slip estimates and uncertainties; the transformation is singular for a N-S oriented fault and optimal for an E-W oriented fault. In contrast to our previous strike-slip estimates, which were based only on a descending interferogram, we now find good agreement with the geological measurements, except at the ends of the rupture. The ascending interferogram reveals significant west-side-down dip-slip (~1.0 m) which reduces the strike-slip estimates by 1-2 m, especially along the northern half of the rupture. A spike in the strike-slip displacement of 6 m is observed in central part of the rupture. This large offset is confirmed by sub-pixel cross-correlation of features in the before and after amplitude images. In addition to strike- and dip-slip, we identify uplift and subsidence along the fault, related to the restraining and releasing bends in the fault trace, respectively. Our main conclusion is that at least two look directions are required for accurate estimates of surface slip even along a "pure" strike-slip fault. Models and results based only on a single look

direction could have major errors. Our new estimates of strike-slip and dip-slip along the rupture provide a boundary condition for dislocation modeling. A simple model, which has uniform slip to a depth of 12 km, shows good agreement with the observed ascending and descending interferograms.

Introduction

Understanding the physics of the earthquake rupture processes, as well as the postseismic rebound following an earthquake, will require a detailed knowledge of the space/time history of slip over a wide range of space and time scales. Here we use the technique of synthetic aperture radar interferometry (InSAR) to measure the co-seismic strike-slip and dip-slip in along the surface of the 1999 Hector Mine rupture (Figure 1). Many publications use InSAR for the recovery of strike-slip displacement following large earthquakes [e.g., *Massonnet et al.,* 1993; 1994; *Zebker et al.,* 1994*; Peltzer et al.*, 1994*; Fujiwara et al.,* 1997*; Michel et al.,* 1999b; *Price,* 1999; *Wright et al.,* 1999]. In addition, vector GPS measurements [*Bock et al.,* 1993; *Johnson et al.,* 1994; *Freymueller et al.*, 1997] have been used in combination with surface slip measurements [*Hudnut et al.,* 1994; *Wald and Heaton*, 1994; *Reilinger et al.,* 2000], and InSAR measurements [*Ozawae et al.,* 1997; *Wright et al.,* 1999] to estimate the 3-D distribution of strike-slip for the 1992 Landers, 1995 Kobe, and 1999 Izmit Earthquakes. Surface slip measurements from field geology [*Sieh et al.,* 1993; *Irvine and Hill,* 1993; *Hart et al.,* 1993; *McGill and Rubin,* 1999] have been used primarily to constrain the strike-slip displacement for the development of full 3-D models [*Wald and Heaton;* 1994]. However, reliable estimates of dip-slip are often not available from field measurements since local geologic and topographic effects can confuse the vertical signal [e.g., *USGS et al.,* 2000]. For example, only one component of near-field displacement was established for the 1992 Landers rupture [*Michel et al.,* 1999b] using a single descending interferometric pair. The ascending pair spanning the event has an unacceptably-long interferometric baseline (~800 m) [*Massonnet and Feigl,* 1998]. *Price* [1999] examined the difference between the model interferogram produced by the *Wald and Heaton* [1994] slip parameters and the observed Landers co-seismic interferogram to estimate dip-slip displacement along the rupture and found vertical displacements of up to a meter were needed to explain the residual interferogram.

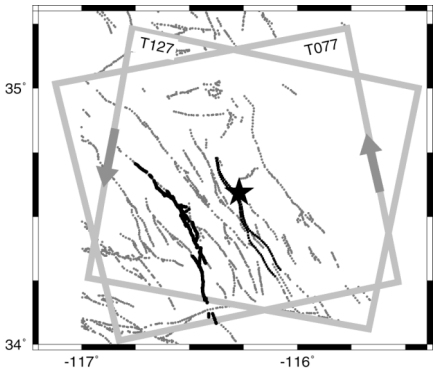

Figure 1

Figure 1. Location map showing frames of ascending (track 077 - T077) and descending (T127) ERS-1/2 radar images. The direction of satellite motion is marked on each frame. The radar looks to the left of the flight line at an average incidence angle of 23° from the vertical. Black dots are are previously mapped faults [*Jennings,* 1994] and solid lines are ruptures of the 1992 Landers earthquake and 1999 Hector Mine earthquake.

Fortunately, both ascending and descending interferograms with are available for the 1999 Hector Mine earthquake so two components of displacement can be measured. In this paper we estimate vector surface slip using only the near-field (< 5 km from the rupture) part of the interferogram. Our objective is to compare these vector slip estimates with field geologic estimates [*USGS et al.,* 2000]. Differences highlight errors with either the InSAR approach or the geologic approach. The surface slip estimates provide a known boundary condition, and thus a starting point, for the development of full 3-D slip models incorporating a variety of data types [e.g., *Wald and Heaton,* 1994]. We show that a very simple model, where slip is uniform from the surface to 12 km depth, provides a good visual fit to the interferograms, in both the near field and far field. The main differences occur in the intermediate field (5-30 km from the rupture) and they reveal factors such as non-uniform slip distribution with depth or slip on fault strands having no surface displacement.

The main strengths of InSAR are the complete spatial coverage, the high spatial resolution (~100-m) and the high ranging precision (2-5 mm) over short distances. The Hector Mine earthquake offers the best interferometric coverage of any event studied so far for the following reasons:

i) Along the descending orbit of ERS-1/2, data were acquired during each of the 4 months prior to the Hector Mine event. This is unusual because, for most parts of the world, a nominal data acquisition schedule is once or twice per year. Unfortunately ascending track coverage is more typical with only one pre-earthquake acquisition in August of 1999 although there are many acquisitions in 1995 and 1996. Since the

orbit of the ERS-2 satellite is controlled in a 2000 m diameter tube it typically takes 20 repeat orbits (700 days) to match a reference orbit to within the desired 100 m baseline. Thus the number of pre-earthquake acquisitions usually determines minimum time span of the interferometric match.

ii) In the case of the Hector Mine earthquake, the descending co-seismic pair has the minimum possible time span of 35 days and it also has an extraordinarily short baseline of only 18 m [*Sandwell et al.,* 2000]. This is not a fluke of statistics but rather an effort by the European Space Agency to control the satellite orbit to optimize data collection for the 1999 Izmit, Turkey earthquake.

iii) The Mojave Desert, with low vegetation and low rainfall, is an ideal surface for retaining interferometric coherence over time spans of 8 years or more. High coherence enables one to probe the shortest wavelengths in the interferometric phase to reveal the details of the rupture [*Price and Sandwell,* 1998]. Moreover, since the region nearby the rupture can experience large accelerations which reduce the coherence, the initially high coherence inherent in the Mojave surface enables one to maintain adequate coherence all the way to the surface rupture [*Michel et al.,* 1999b].

iv) Finally, the precision orbit determination for ERS-1/2 is optimal over North America because of the accurate tracking by satellite laser ranging stations [*Scharoo and Visser,* 1998]. Because these precise orbits are readily available, it is unnecessary to flatten the interferometric phase measurements. Flattening of the phase without using, for example precise, GPS control points, could remove part of the long-wavelength co-seismic deformation signature and lead to inaccurate and inconsistent results.

Indeed, it is unlikely that such an optimal interferometric image of a large earthquake will occur in the next decade, especially given the current plans for future SAR missions.

We use the gradient of the interferometric phase to delineate the surface rupture as shown in Figure 2 from *Sandwell et al.,* [2000]. The yellow dots in this figure are the surface traces of previously mapped faults [*Jennings*, 1994]. The dark red line is the surface rupture of the 1992 Landers Earthquake [*Sieh et al.,* 1993]. The main surface rupture of the Hector Mine event was mapped by a team of field geologists [*USGS et al.*, 2000]; it lies between the red dotted lines in Figure 2. The thin dashed white lines mark the mean slip direction as determined by GPS measurements in the far field [*Hurst et al.*, 2000]. The shading in the image represents the

phase gradient, which saturates at ± 1 radian per pixel; this corresponds to a strain $2.x10^{-4}$ or approximately the elastic strain limit of rocks. Thus areas of saturation of the grey scale (black or white) reveal areas of surface faulting. We have identified the outer limits of the main rupture zone using this phase gradient map, along with the geologic map of the surface rupture. The northern end of the rupture zone is about 500 m wide while the central area is about 1 km wide and the southern area is about 5 km wide. Our objective is to estimate the total strike-slip and dip-slip displacements across this rupture zone and compare this with geological estimates. Disagreement could be related to measurement error, to fault-normal displacement, or simply be attributed to the different definitions of the rupture zone.

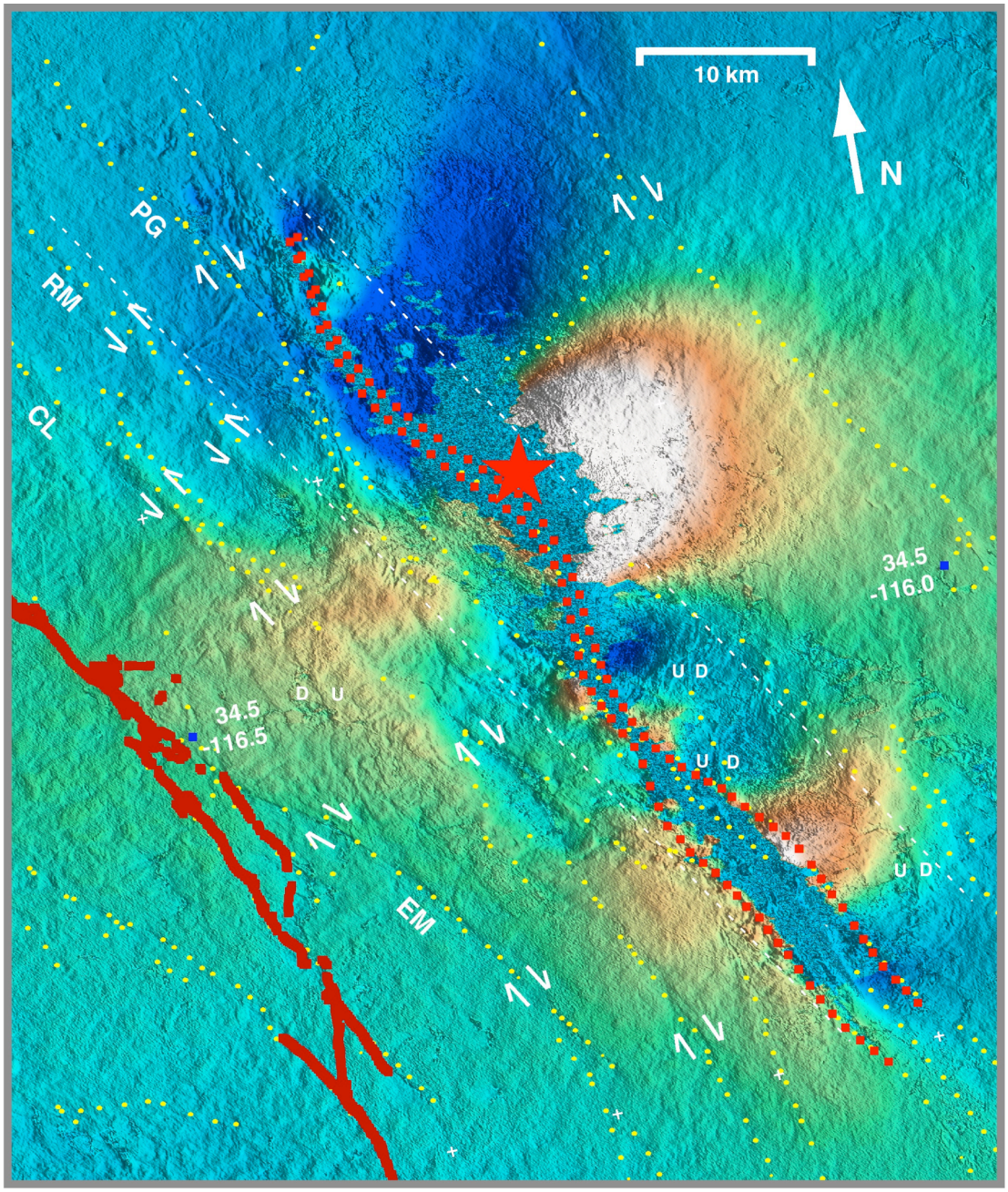

Figure 2

Figure 2. East component of phase gradient [*Sandwell et al.,* 2000] derived from descending co-seismic interferogram. Colors represent line of sight displacement toward the radar with a preliminary model removed (Figure 7). Yellow dots are previously mapped faults [*Jennings,* 1994] and the dark red line is the surface rupture of the 1992 Landers earthquake [*Sieh et al.,* 1993]. Red squares, spaced at approximately 1-km intervals, represent the outer boundary of the zone of complex faulting seen in the phase gradient. The thin white dashed lines mark the strike of the rupture determined from far-field GPS measurements [*Hurst et al.,* 2000]. Also note that lineaments in phase gradient away from the main rupture follow previously mapped faults and represent small amounts of triggered slip in both right-lateral Emerson Fault (EM) and left-lateral

directions [Calico (CL) and Rodman (RM)]. Most of the triggered slip lies between the Landers and Hector Mine ruptures. Significant surface disruption occurs along the Pisgah Fault (PG).

Previous InSAR estimates of surface slip

In a previous publication, *Sandwell et al.,* [2000] compared slip estimates from InSAR with the geologic estimates (Figure 3). The InSAR estimate was based on a single descending interferogram. The approach and assumptions follow: 1) Select a zero phase point far from the rupture. 2) Select two paths through the interferogram from the common zero point to conjugate points across the fault. 3) Count fringes from the zero point to the conjugate points. The advantage of this approach over computer phase unwrapping is that one can estimate fringe rate in noisy areas and apply a subjective fringe-counting uncertainty. The result is line-of-sight (LOS) displacement on each side of the fault, which can be differenced to obtain LOS difference across the fault (Figure 3, dashed line). 4) Finally, assume pure strike-slip displacement and use the fault orientation and the LOS unit vector to estimate the strike-slip displacement (Figure 3, solid line).

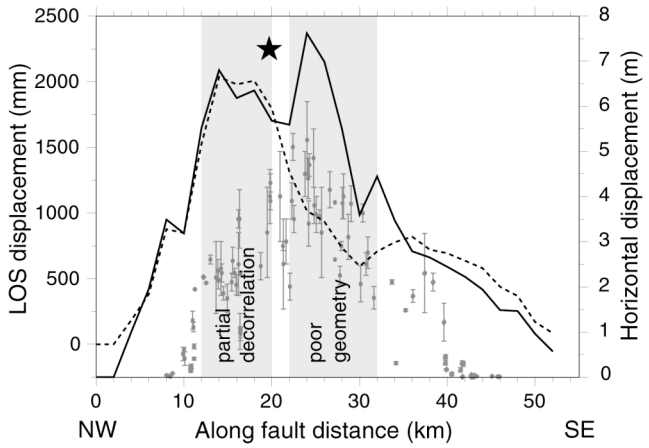

Figure 3

Figure 3. Line of sight (LOS) surface displacement seen in descending interferogram established by counting interferometric fringes to the west and east outer rupture zones, respectively. dashed line is west LOS minus east LOS. Assuming no vertical displacement, and accounting for fault orientation and look geometry, *Sandwell et al.* [2000] provide estimates of strike-slip displacement that are significantly greater than geological estimates [gray points, *USGS et al.,* 2000]. The length of the rupture zone determined from the phase gradient (Figure 2) is 12 km greater than the geologic estimate.

These preliminary results showed poor agreement with the geologic slip estimates; the InSAR slip estimates are 1-2 m greater than the geologic measurements. As noted by *Sandwell et al.,* [2000] there were two possible explanations for the difference. First, the field geologists could have underestimated the total displacement because they missed many small-offset faults off the main rupture. Second, there could be significant dip-slip component with the west-side-down so

the pure strike-slip assumption is incorrect. Since the geologic estimates of dip-slip displacement are highly scattered, *Sandwell et al*. [2000] favored the first explanation. Here we resolve the issue by adding the LOS vector from an ascending co-seismic interferogram that became available in March of 2000.

Vector Slip from InSAR

The objective is to use line-of-sight (LOS) displacement measurements from ERS InSAR to estimate strike-slip and dip-slip displacements along the rupture. We consider an arbitrary vector displacement $\Delta\mathbf{x}$ at a vector position $\mathbf{x}_f$ along the fault and assume that the component of displacement perpendicular to the local fault plane is zero.

$$\Delta\mathbf{x} \bullet \mathbf{e} = 0 \qquad (1)$$

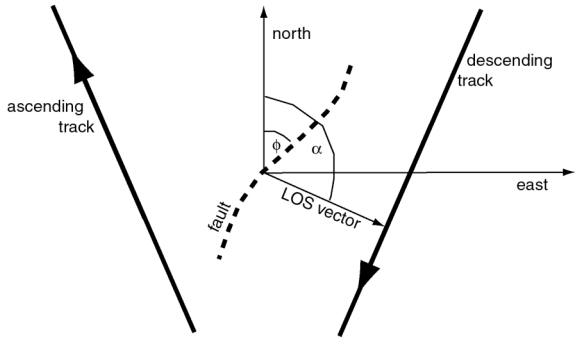

Figure 4

Figure 4. Geometry of ascending and descending ERS satellite tracks and look vectors in relation to the surface trace of the fault. ϕ is the azimuth of the fault trace and α is the azimuth of the look vector.

The ERS satellite can view this displacement from two positions $\mathbf{x}_a$ and $\mathbf{x}_d$ along ascending and descending orbits, respectively (Figure 4). The interferogram measures the LOS range change (Δl_a and Δl_d) from these two positions. The LOS vector from the displaced point to the satellite (ascending orbit) is $\mathbf{x}_a$ - $\mathbf{x}_f$. The LOS displacement is then the dot product of this unit vector $\mathbf{e}_a$

$$\Delta l_a = -\Delta\mathbf{x} \bullet \frac{\left(\mathbf{x}_a - \mathbf{x}_f\right)}{\left|\mathbf{x}_a - \mathbf{x}_f\right|} = -\Delta\mathbf{x} \bullet \mathbf{e}_a \qquad (2)$$

with the negative of the displacement vector.

Similarly, the LOS displacement can be measured along the descending pass so we have three equations and three unknowns.

$$\begin{bmatrix} 0 \\ \Delta l_a \\ \Delta l_d \end{bmatrix} = \begin{bmatrix} e_1 & e_2 & e_3 \\ -e_{a_1} & -e_{a_2} & -e_{a_3} \\ -e_{d_1} & -e_{d_2} & -e_{d_3} \end{bmatrix} \begin{bmatrix} \Delta x \\ \Delta y \\ \Delta z \end{bmatrix} \qquad (3)$$

Next we write expressions for all three unit vectors. Select a local co-ordinate system with an origin at the fault, $\mathbf{x}_f$ and the x, y, and z-axes oriented east, north, and up, respectively. Looking downward along the z-axis (Figure 4) we would see the fault trace as well as the ground tracks of the ascending and descending orbits.

The important angles are the fault azimuth ϕ and the azimuth of the LOS vector α (103˚ for a descending ERS track and -103˚ for an ascending track at this latitude). Assume that the fault is vertical so e_3 is zero. Note this assumption is not necessary but it is appropriate in this case. The first row of the unit vector matrix is $\cos\phi$, $\sin\phi$, 0. Next calculate the unit vectors for the two look directions. These are

$$\begin{bmatrix} e_{a_1} \\ e_{a_2} \\ e_{a_3} \end{bmatrix} = \begin{bmatrix} -\sin\alpha\sin\theta \\ \cos\alpha\sin\theta \\ \cos\theta \end{bmatrix} \quad \text{and} \quad \begin{bmatrix} e_{d_1} \\ e_{d_2} \\ e_{d_3} \end{bmatrix} = \begin{bmatrix} \sin\alpha\sin\theta \\ \cos\alpha\sin\theta \\ \cos\theta \end{bmatrix} \qquad (4)$$

where θ is the look angle (23˚ for ERS in the center of the frame). Assuming a vertical fault plane, and letting Δs be the strike-slip component of slip we find

$$\Delta x = \Delta s \sin\phi$$

$$\Delta y = \Delta s \cos\phi. \qquad (5)$$

Substituting Δx and Δy into the system of equations we find.

$$\begin{bmatrix} \Delta l_a \\ \Delta l_d \end{bmatrix} = \begin{bmatrix} \sin\alpha\sin\theta\sin\phi - \cos\alpha\sin\theta\cos\phi & -\cos\theta \\ -\sin\alpha\sin\theta\sin\phi - \cos\alpha\sin\theta\cos\phi & -\cos\theta \end{bmatrix} \begin{bmatrix} \Delta s \\ \Delta z \end{bmatrix} \quad (6)$$

Now we have two measurements and two unknowns of the form **b = Ax** and all of the usual matrix machinery can be used to solve for Δx, Δz as well as their uncertainties. One important issue is the possibility of a singular **A**-matrix. This occurs when the determinant of **A** is zero.

$$|\mathbf{A}| = -2\sin\alpha\sin\phi\sin\theta\cos\theta \quad (7)$$

The determinant of **A** is

There are three singular cases:

i) $\theta = 0$ vertical look angle,

ii) $\alpha = 0$ equatorial orbit, and

iii) $\phi = 0$ N-S trending fault.

The third possibility is important for the Hector Mine rupture because the central part of the rupture is oriented almost due north.

New Slip Estimates

Using this purely geometric approach we estimate the surface slip vector for the Hector Mine rupture. The ascending and descending interferograms are shown in Figure 5. Due to the lack of ascending data acquisitions prior to the Hector Mine event, the quality of the ascending interferogram is not ideal. The time span between the reference and repeat images is 4 years, the repeat image was collected 71 days after the rupture (i.e., mildly contaminated by post-seismic displacement of a few centimeters [*Jacobs et al., this issue*]), and the perpendicular baseline is not optimally short (i.e., ~60 m). To remove the interferometric fringes, the United States Geological Survey (USGS) 90-m topography was used to help unwrap the phase of an ERS-1/2 tandem pair (195-m perpendicular baseline). While the ascending interferogram is generally noisy due to its long time span, the interferometric fringes are relatively clear except on the northeast side of the rupture where severe ground shaking degrades the correlation. In contrast,

the descending co-seismic interferogram has far less decorrelation due to is short baseline (18 m) and the short 35-day time span between the reference and repeat images.

To improve the fringe clarity in areas of high displacement gradient and partial correlation due to ground shaking, we used a two-step process to construct the final interferograms. First we formed an interferogram using the standard approach which has minimal filtering of the complex numbers. (We use a Gaussian filter with a 0.5 gain at a full wavelength of 84 m to suppress noise.) Fringes were counted and slip was estimated as described above. These preliminary slip estimates were used to compute LOS phase for both ascending and descending interferograms. Second, we recomputed the interferograms while removing the phase models. Removal of this crude model, greatly reduced the fringe rate which makes it possible to increase the spatial filtering from the nominal 84-m cutoff-wavelength to a 170-km cutoff wavelength. This approach greatly improved fringe clarity, especially in areas of partial decorrelation since the coherence increases with increasing wavelength [*Sandwell and Price*, 1998]. We note that this two-step process also reduces the magnitude of the phase gradient, enabling one to "see" phase gradient signatures (Figure 2) closer to the rupture zone than was shown by *Sandwell et al.* [2000]. Finally, to further improve fringe clarity, the repeat images were shifted by 1-3 m in azimuth to accommodate the motion of the ground [*Michel et al.,* 1999b]. This only provided improvement in fringe clarity in the areas where slip exceeded about 4 m.

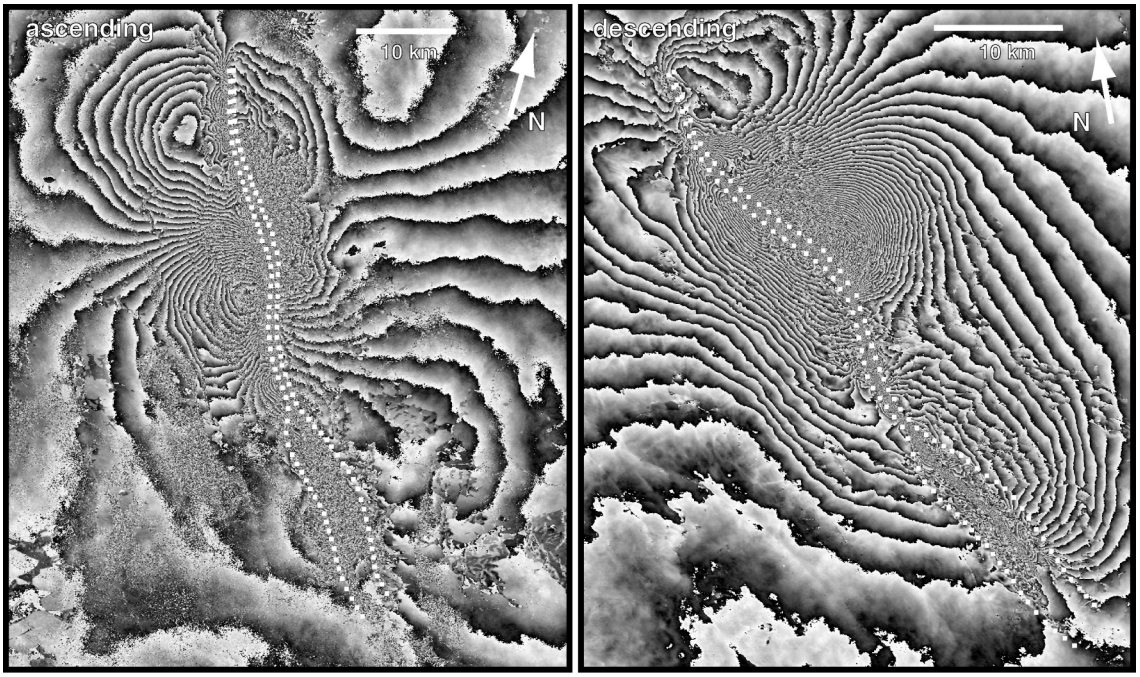

Figure 5

Figure 5. (left) Interferogram formed from ascending ERS SAR data (e1_23111, e2_24480). The timespan between the reference and repeat images is 4 years, the repeat image was collected 71 days after the October 16 rupture, and the perpendicular baseline is 60 m. The USGS 90-m topography was used to help unwrap the phase of a long baseline (195 m) topographic pair. While the interferogram is generally noisy due to its long timespan, the interferometric fringes are relatively clear except on the northeast side of the rupture where severe ground shaking causes decorrelation. The interferogram was not flattened.
(right) Interferogram formed from descending ERS SAR data (e2_23027, e2_23528). The timespan between the reference and repeat images is only 35 days, the repeat image was collected 4 days after the October 16 rupture and the perpendicular baseline is only 18 m. These factors contribute to overall excellent correlation except in the region of severe ground shaking. The interferogram was not flattened.

As described above, fringes were counted from a common zero point (same location in each interferogram) to conjugate points across the rupture. This resulted in two LOS displacement estimates for each interferogram (Tables 1 and 2) as shown Figure 6B and C. Counting errors were estimated visually. The largest counting uncertainties are along the northern half of the east strand (15-22 km in Figure 6B).

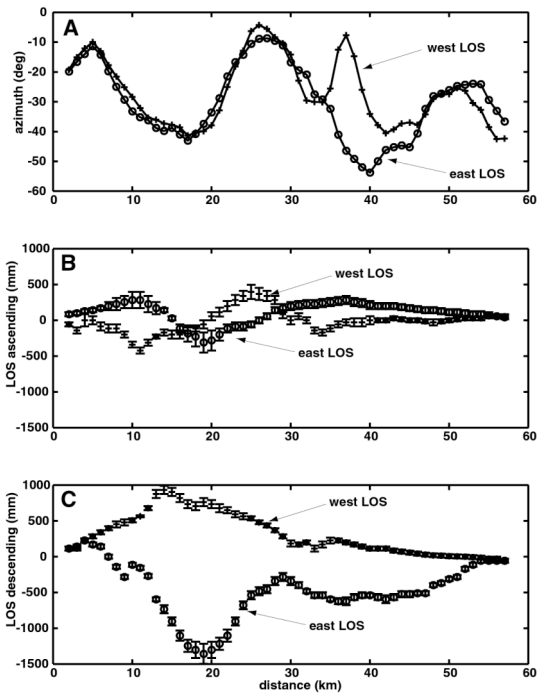

Figure 6

Figure 6. (A) Azimuth of west and east outer boundaries of the rupture zone. (B) LOS displacement and error estimates along west and east outer boundaries of rupture zone determined by counting fringes in ascending interferogram from a common zero point far from the rupture. (C) Estimate of displacement and error for descending interferogram.

It should be emphasized that the interferograms were not flattened since flattening could introduce inconsistencies in the LOS displacements. Simple arguments suggest that flattening is unnecessary. Absolute ERS orbit error is typically less than 100 mm so the orbit error difference should be √2 greater or ~140 mm [*Scharroo and Visser,* 1998]. Because the height of the spacecraft is seven times the width of the radar swath, this cross-track orbit error maps into only 20 mm of LOS error across a 100 km-wide swath. There can also be an along-track error related to the change in relative orbit error along the 100-km frame. This is more difficult to estimate but it should be much less than 20 mm. Because the Hector Mine rupture is only 50 km long, the LOS tilt errors should be less than 10 mm or 1/3 of a fringe. These errors are less than the typical counting error of 1/2 fringe. Our experience shows that large tilts (i.e. more than 40 mm over 100 km) in the interferogram are related to either inconsistencies in the geodetic model for the Earth and orbit or they are due to time-tag errors in the ERS leader files. This can be avoided by using the time-tag information appended to each radar echo.

In addition to the 4 LOS measurements, the azimuth of the rupture is needed to estimate the vector slip. Since the outer boundaries of the rupture zone are not parallel, especially at the southern end of the rupture, we estimated a smooth azimuth along each strand independently (Figure 6, top). The strike-slip and dip-slip displacement for the east and west strands are computed independently by inverting equation 6 at each of the 56 points along the two strands. Errors in slip are determined from the diagonal elements of the inverse of the $\mathbf{A}^T\mathbf{A}$ matrix where each equation is first divided through by the appropriate LOS error estimate. The results are independent estimates of strike- and dip-displacement on the east and west sides of the faults (Tables 1 and 2). We subtract these displacements (west - east) to isolate the strike-slip and dip-slip part of the solution as shown in Figure 7. The sum of the two displacements reveals the component of displacement that is common across the fault as shown in Figure 8.

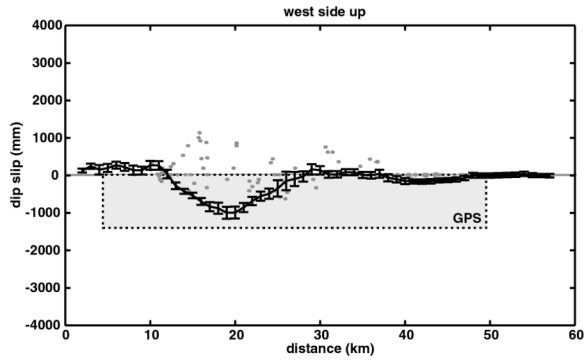

Figure 7

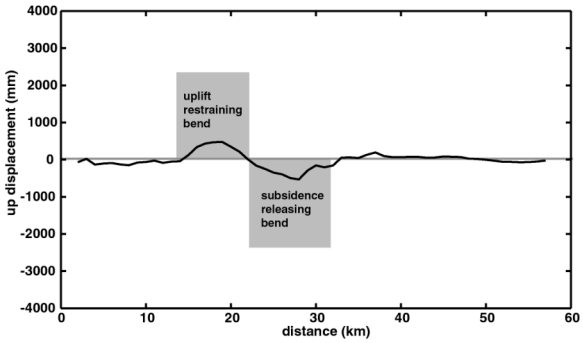

Figure 8

Figure 7. (top) Estimate of dip-slip displacement and uncertainties along the rupture zone compared with geologic [gray points, *USGS et al.,* 2000] and far-field GPS [dashed line, *Hurst et al.,* 2000] estimates. Note the prominent west-side-down slip between distances of 12 and 25 km along the rupture from the InSAR analysis. This vertical component, which was not accounted for in the estimate by *Sandwell et al.*, [2000], resulted in a significant overestimate of horizontal slip (Figure 3). (bottom) New InSAR estimate of strike-slip displacement along with geologic and GPS estimates. There is now good agreement between distances of 17 km and 41 km. The grey circle is an independent confirmation of strike-slip offset derived from cross-correlation of amplitude images from before and after the earthquake.

Figure 8. The components of LOS displacement that are common to conjugate points across the fault are rotated into along-strike displacement (bottom) and up displacement (top). Note that it is probable that the fault normal displacement at the surface is not zero as assumed here. For this 2-D interpretation of 3-D data, there is uplift at the restraining bend in the fault and subsidence at the releasing bend. The along-strike motions imply dilatation near the center of the rupture where we see evidence for normal faulting (Figure 2). This along-strike displacement may be evidence for a deep northern-trending rupture that intersects the main rupture at a distance of about 20 km.

Strike-slip and dip-slip displacement

By including the information from the ascending interferogram, the strike-slip results are now in much better agreement with the geologic measurements of slip (gray points in Figure 7) than in our previous publication [*Sandwell et al*., 2000]. The agreement is especially good between 17 km and 40 km along the rupture. The maximum InSAR slip estimate is now 6.07 $\pm$ 2.17 m while the maximum geologic slip is 5.25 $\pm$ 0.85 m. Our previous maximum estimate was much larger [7.7 m; *Sandwell et al.,* 2000]. The main difference between the new and old InSAR estimates occurs between 10 and 25 km along the rupture, where the new estimates are 2 meters lower and in better agreement with the geologic estimates. The reason for the lower strike-slip estimate is that there is a significant west-side-down dip-slip displacement. This is partially confirmed by the far-field GPS measurements (dashed line , Figure 7) although the InSAR measurements indicate much smaller overall vertical slip. Since the look angle of ERS is only 23 degrees from vertical, ignoring this small vertical component resulted in a large strike-slip error in our previous estimate. Although there is now generally good agreement in the strike-slip displacement over the center two thirds of the rupture, the InSAR estimates are systematically greater. The greatest disagreements are along the along the northern and southern ends of the rupture where the InSAR estimates are 1-2 m greater than the geological estimates. The discrepancy at the southern end is expected because of the complex zone of faulting, and perhaps distributed shear, found between two fault strands. At the northern end of the rupture, a clear offset in phase is apparent in both interferograms suggesting the InSAR offset is accurate.

The main discrepancy between the InSAR and geologic estimates now lies in the dip-slip component. Here the interferograms reveal a systematic variation of dip-slip along the rupture reaching a magnitude of -1.03 $\pm$ 0.175 m. Indeed the uncertainties in the dip-slip are three times smaller than the strike-slip uncertainties because of the steep look geometry of ERS. The geologic estimates of dip-slip displacement are scattered and probably reflect very local effects

rather than the main basement faulting. The published [*Hurst et al.*, 2000] 8-parameter GPS inversion requires -1.45±0.18 m of dip-slip which it inconsistent with both the InSAR and geologic observations and we expect the more comprehensive set of GPS observations closer to the rupture will show better agreement with the InSAR dip-slip displacement estimates.

As a final check on the strike-slip estimates, we use the amplitude-offset method of *Michel et al.*, [1999a] to estimate the azimuth displacement in the descending interferogram (Figure 9). Amplitude offsets vary between ±3 m and show qualitative agreement with the strike-slip estimates. The central part of the rupture is oriented nearly parallel to the satellite track so it is a direct measure of strike-slip displacement. One azimuth-offset profile across the fault (Figure 9, top) has 6 m of displacement in agreement with the InSAR estimate (large gray/white circle in Figure 7).

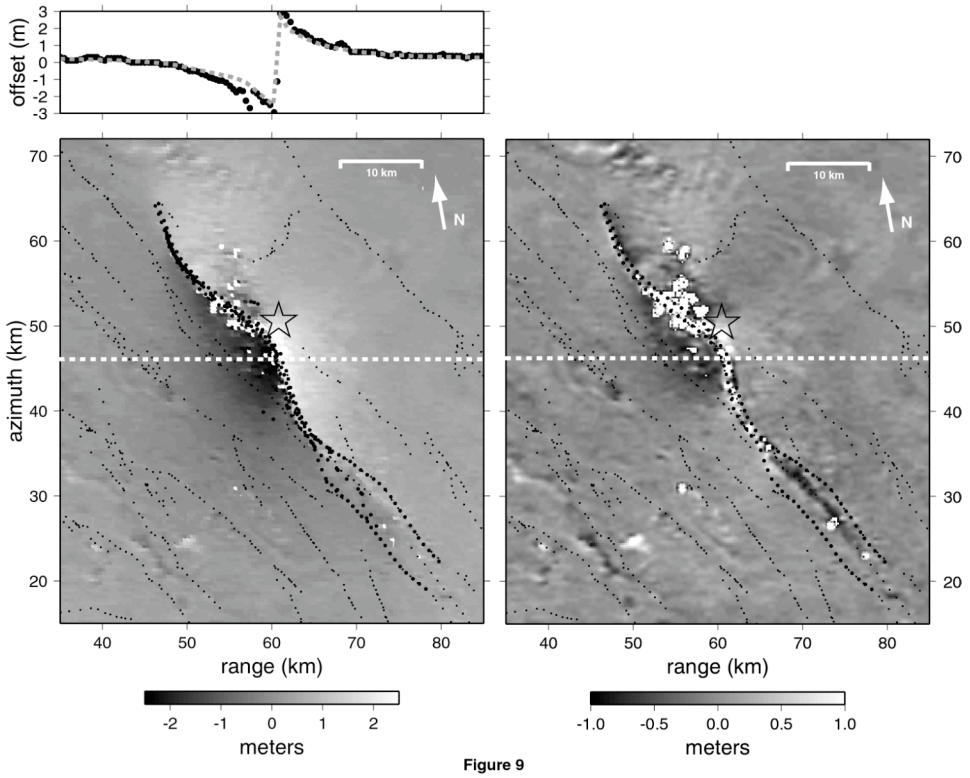

Figure 9

Figure 9. (left) Azimuth offsets determined by amplitude cross correlation [*Michel et al.*, 1999a] provide a crude measure (~ 200 mm accuracy) of the horizontal motion of the surface. This component lies at an azimuth of 13˚ along the descending satellite track. Southwest offsets of up to 3 m appear on the east side of the rupture while the west side shows NW motion. A profile at an azimuth of 47 km (dashed line) reveals a maximum strike-slip displacement of 6 m in agreement with the interferometric and geologic estimates shown in Figure 7.
(right) Residual azimuth offsets from the strike-slip and dip-slip displacement model shown in Figure 7. The model assumes uniform slip with depth to 12 km and zero slip below 12 km. Deviations from the model are typically less than 1 meter. Azimuth offsets were not used to estimate fault slip so this is a completely independent check of the model.

Common-mode displacement

A novel aspect of our approach is the ability to measure two of the three displacement components that are common to both sides of the fault. Common-mode displacement could also be measured with GPS, however, it is rare to have a GPS receiver within 1 km the rupture prior to the earthquake. Moreover, one would need two GPS receivers at conjugate points across the fault to distinguish the common-mode displacement from strike-slip or dip-slip displacement. Two components of common displacement are shown in Figure 8. Vertical uplift (Figure 8, top) occurs between 13 and 21 km along the fault while vertical subsidence occurs between 21 and 32 km along the fault. These two zones of uplift and subsidence correspond to the restraining and releasing bends along the rupture, respectively (Figure 1). The horizontal measurements show that the northern 1/3 of the fault moved about 1 m northwest while the southern 2/3 moved about 1 m southeast. This may be evidence for a surface displacement contribution due to an additional buried fault.

For a straight fault in a linear elastic half-space with no slip on nearby faults, this common-mode component should be zero but it is not. We will explore the common mode in a later publication although preliminary results indicate that it is due to a curved rupture and that non-linear elasticity is not required by the observations [*Peltzer et al.,* 1999]. (Note that the assumption of zero fault-normal displacement does not apply to the common mode displacement so our two-component interpretation is not valid and the uncertainties in these estimates are unknown.)

Preliminary Models

Given this boundary condition on the surface vector slip, the next step is to integrate the other geodetic data and the full interferogram(s), to determine slip at depth as well as to determine the need for significant slip on nearby buried faults [*Fialko et al*., 2001]. As a first step we have extended the surface strike- and dip-slip models (Figure 7) to a depth of 12 km and computed synthetic interferograms using an elastic half-space formulation [*Feigl and Dupre*, 1999; *Okada*, 1985]. The results (Figure 10) show good agreement with the interferometric fringes in the near field and also in the far field but the fit at intermediate distances between 5 and 30 km from the rupture is sometime poor. We expect much better agreement with the intermediate-distance

displacement by adjusting the slip distribution with depth. The same model was used to compute the azimuth offsets shown in Figure 9; residuals are generally less than 0.3 m. Since the azimuth offsets were not used to estimate the fault-slip, this is an independent check of the LOS analysis.

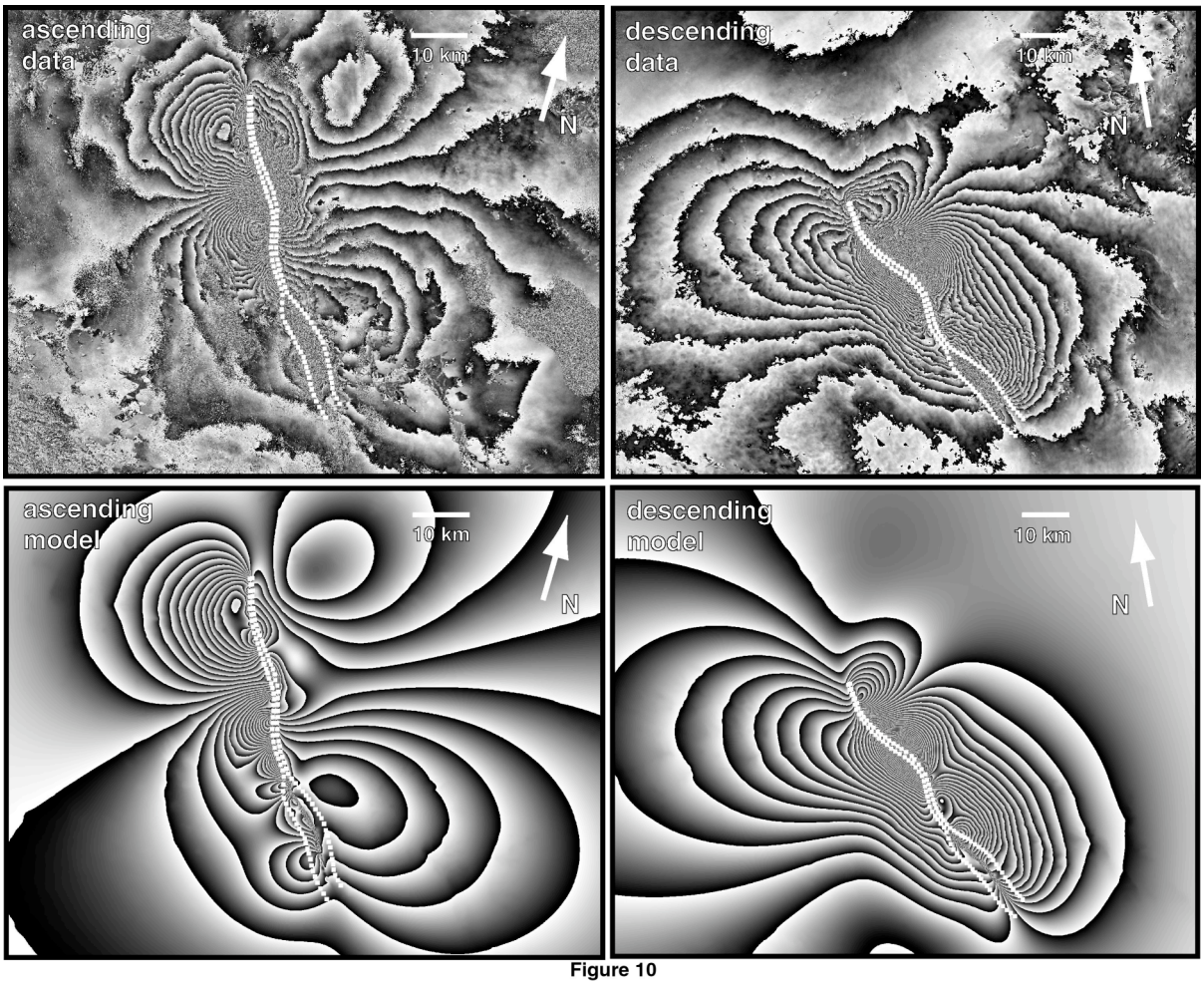

Figure 10

Figure 10. Preliminary models of the ascending and descending interferogram using the strike-slip and dip-slip values and uniform slip between the surface and 12 km [*Feigl and Dupre,* 1999; *Okada,* 1985]. The good visual agreement suggests that complicated depth variation in slip is not required by the observations.

LOS residuals from the descending interferogram (colors in Figure 1) show evidence for right-lateral slip on the Pisgah Fault, which is 5 km west of the northern end of the main rupture. As noted in *Sandwell et al*. [2000], the Calico and Rodman faults display evidence for left-lateral triggered slip. The west sides of these faults moves toward the radar and there is a corresponding lineament in the phase gradient (Figure 2). Triggered slip on faults to the south is consistent with the expected right-lateral motion. Large LOS residuals occur on the east side of the rupture (colors in Figure 1) suggesting there is significant slip on a northward trending fault in the

vicinity of the epicenter [*Fialko et al*., 2001. These LOS residuals at intermediate distances from the rupture provide information that is only available in the InSAR data and thus further analysis is warranted. In particular, it is important to determine whether or not non-linear crustal rheology is required by the geodetic data as in the case of the Manyi (Tibet) Earthquake [*Peltzer et al*., 1999].

Conclusions

Our main conclusion is that at least two radar look directions are needed to provide reliable estimates of slip along a rupture, even in areas where geological information suggests a pure strike-slip mechanism. For depths in the Earth greater than about 1 kilometer, the normal component of stress on a fault (>15 MPa) is significantly greater than the typical stress drop during an earthquake (~5 MPa). Thus it seems reasonable to assume the fault normal displacement at depths greater than 1 km will be much smaller than the strike-slip or dip-slip displacements. The interferometric coverage of the Hector Mine rupture zone is adequate for estimating line-of-sight displacement to within a few kilometers of the rupture. Under these assumptions, we find reasonably good agreement between strike-slip displacement estimates from InSAR and geological estimates. Since geologists measure the offset directly above the fault and the InSAR measurements do not extend into the zone of complex surface faulting, one would not expect perfect agreement. InSAR-derived offsets are typically larger than the geological estimates. Finally, we note that a simple model with surface slip extended to 12 km depth, fits the far-field areas of the interferograms remarkably well but large discrepancies remain in the intermediate field (5-30 km). Refinements of this model will hopefully provide robust estimates in the depth variation of slip.

Acknowledgements. Our SAR processing software is based on the Stanford/JPL algorithms for image focussing and precise alignment provided by Howard Zebker. SAR data were provided by the European Space Agency through its distributors SpotImage and Eurimage. The research was funded by the Southern California Eathquake Center and the National Science Foundation (EAR-0105896 and EAR-9977823).

REFERENCES

Bock, Y. D. Agnew, P. Fang, J. Genrich, B. Hager, T. Herring, K. Hudnut, R. King, S. Larson, J.-B. Minster, K. Stary, S. Widowinski, and F. Wyatt, Detection of crustal deformation related to the Landers earthquake sequence using continuous GPS measurements, *Nature, 361*, no. 6410, 337-340, 1993.

Feigl, K.L., and E. Dupre, RNGCHN: a program to calculate displacement components from dislocations in an elastic half-space with applications for modeling geodetic measurements of crustal deformation, *Comput. Geosci., 25* (6), 695-704, 1999.

Fialko, Y., M. Simons, and D. Agnew, The complete (3-D) surface displacement field in the epicentral area of the 1999 Mw7.1 Hector Mine earthquake, California, from space geodetic observations, Geophys. Res., Lett., 28 (16), 3063-3066, 2001.

Freymuller, J., N.E. King, and P. Segall, The co-seismic slip distribution of the Landers earthquake, *Bull. Seism. Soc. Am.*, *84* (3), 646-659, 1994.

Fujiwara, S., P. A. Rosen, M. Tobita, and M. Murakami, Crustal deformation measurements using repeat-pass JERS-1 synthetic aperture radar interferometry near the Izu Peninsula, Japan, *J. Geophys. Res., 103*, 2411-2426, 1997.

Hart, E.W., W.A. Bryant, and J.A. Treiman, Surface faulting associated with the June 1992 Landers earthquake, California, *Calif. Geol.*, *46*, 10-16, 1993.

Hudnut, K.W., and 16 others, Co-seismic displacements of the 1992 Landers earthquake sequence, *Bull. Seism. Soc. Am.*, *84* (3), 625-645, 1994.

Hurst, KJ; Argus, DF; Donnellan, A; Heflin, MB; Jefferson, DC; Lyzenga, GA; Parker, JW; Smith, M; Webb, FH; Zumberge, JF. The coseismic geodetic signature of the 1999 Hector Mine Earthquake. Geophys. Res. Lett., *27*(N17), 2733-2736, 2000.

Irvine, P.J., and R. L. Hill, Surface rupture along a portion of the Emerson fault, *Calif. Geol.*, *46*, 23-26, 1993.

Jennings, C. W., Fault activity map of California and adjacent areas with locations and ages of recent volcanic eruptions, map scale 1:750,000, Department of Conservation, 1994.

Johnson, H.O., D.C. Agnew, and K. Hudnut, Extremal bounds on earthquake movement from geodetic data: Application to the Landers earthquake, *Bull. Seism. Soc. Am.*, *84* (3), 660-667, 1994.

Massonnet, D., M. Rossi, C. Carmona, F. Adragna, G. Peltzer, K. Feigl, and T. Rabaute, The displacement field of the Landers earthquake mapped by radar interferometry, *Nature*, *364* (8 July), 138-142, 1993.

Massonnet, D., K. Feigl, M. Rossi, and F. Adragna, Radar interferometric mapping of deformation in the year after the Landers earthquake, *Nature, 369*, 227-230, 1994.

McGill, S.F., and C. M. Rubin, Surficial slip distribution on the central Emerson fault during the June 28, 1992, Landers earthquake, California, *J. Geophys. Res., 104* (B3), 4,811-4,834, 1999.

Michel, R; Avouac, JP; Taboury, J. Measuring near field coseismic displacements from SAR images: application to the Landers earthquake, Geophys. Res., Lett., *26* (N19), 3017-3020, 1999a.

Michel, R; Avouac, JP; Taboury, J. Measuring ground displacements from SAR amplitude images: application to the Landers earthquake, Geophys. Res. Lett, *26* (N7), 875-878, 1999b.

Murray, M.H., J.C. Savage, M. Lisowski, and W.K. Gross, Coseismic displacements: 1992 Landers, California, earthquake, *Geophys. Res. Lett., 20,* 623-626, 1993.

Okada, Y., Surface deformation to shear and tensile faults in a half-space, *Bull. Seismol. Soc. Am., 75* (4), 1135-1154, 1985.

Ozawa, S., m. Murakami, S. Fujiwara and M. Tobita, Synthetic aperture radar interferogram of the 1995 Kobe earthquake and it geodetic inversion*, Geophys. Res. Lett., v. 24*, no. 6, p. 707-710, 1997.

Peltzer, G., K.W. Hudnut, and K.L. Feigl, Analysis of coseismic surface displacement gradients using radar interferometry: New insights into the Landers earthquake, *J. Geophys. Res.*, *99* (B11), 21,971-21,981, 1994.

Peltzer, G, F. Crampe, and G. King, Evidence of nonlinear elasticity of the crust from the Mw7.6 Manyi (Tibet) earthquake, *Science, 286* (N5438), 272-276, 1999.

Price, E.J. and D.T. Sandwell, Small-scale deformations associated with the 1992 Landers, California, earthquake mapped by synthetic aperture radar interferometry phase gradients, *J. Geophys. Res., 103* (B11), 27,001-27,016, 1998.

Price, E. J., Coseismic and postseismic deformation associated with the 1992 landers, California, earthquake measured by synthetic aperture radar, Ph. D. thesis, Scripps Institution of oceanography, La Jolla, CA, pp. 67-122, 1999.

Reilinger, RE; Ergintav, S; Burgmann, R; McClusky, S; Lenk, O; Barka, A; Gurkan, O; Hearn, L; Feigl, KL; Cakmak, R; Aktug, B; Ozener, H; Toksoz, MN. Coseismic and postseismic fault slip for the 17 August 1999, M=7.5, Izmit, Turkey earthquake *Science*, *289* (N5484), 1519-1524, 2000.

Sandwell, D. T. and E. J. Price, Phase gradient approach to stacking interferograms, *J. Geophys. Res., 103*, 30183-30204, 1998.

Sandwell, D. T., L. Sichoix, D. Agnew, Y. Bock, and J-B. Minster, Near-real-time radar interferometry of the Mw 7.1 Hector Mine Earthquake, *Geophys. Res., Lett., 27*, 3101-3104, 2000.

Sieh, K., L. Jones, E. Hauksson, K. Hudnut, D. Eberhart-Phillips, T. Heaton, S. Hough, K. Hutton, H. Kanamori, A. Lilje, S. Lindvall, S.F. McGill, J. Mori, C. Rubin, J.A. Spotila, J. Stock, H.K. Thio, J. Treiman, B. Wernicke, J. Zachariasen, Near-Field Investigations of the Landers Earthquake Sequence, April to July 1992, *Science*, *260* (9 April), 171-176, 1993.

Scharroo, R., P. Visser, Precise orbit determination and gravity field improvement for the ERS satellites*, J. Geophys. Res., 103,* 8113-8127, 1998.

U.S. Geological Survey, the Southern California Earthquake Center, and the California Division of Mines and Geology, Preliminary Report on the 16 October 1999 M7.1 Hector Mine, California, Earthquake, *Seismol. Res. Lett., 71,* 11-23, 2000.

Wald, D.J., and T.H. Heaton, Spatial and temporal distribution of slip for the 1992 Landers, California, earthquake, *Bull. Seism. Soc. Am.*, *84* (3), 668-691, 1994.

Wright, TJ; Parsons, BE; Jackson, JA; Haynes, M; Fielding, EJ; England, PC; Clarke, PJ. Source parameters of the 1 October 1995 Dinar (Turkey) earthquake from SAR interferometry and seismic bodywave modelling, *Earth, Planet. Sci. Lett., 172*, 23-37, 1999.

Zebker, H.A., P.A. Rosen, R.M. Goldstein, A. Gabriel, and C.L. Werner, On the derivation of coseismic displacement fields using differential radar interferometry: The Landers earthquake, *J. Geophys. Res.*, *99* (B10), 19,617-19,643, 1994.

Table 1. Surface Slip - eastern strand

			ascending		descending		strike		dip	
longitude	latitude	azi.	los	σ	los	σ	slip	σ	slip	σ
-116.3725	34.7203	-19.9	85	28	113	28	109	154	-98	26
-116.3693	34.7110	-16.6	99	28	141	28	195	184	-113	27
-116.3660	34.7025	-14.0	127	28	226	28	536	217	-142	30
-116.3640	34.6936	-11.4	141	28	170	28	188	266	-151	33
-116.3615	34.6841	-14.3	170	28	141	28	-151	213	-183	29
-116.3584	34.6756	-19.8	198	57	0	28	-767	245	-176	51
-116.3542	34.6673	-25.0	226	85	-141	28	-1144	278	-145	69
-116.3495	34.6598	-29.3	255	85	-283	28	-1441	240	-105	66
-116.3438	34.6520	-33.3	283	113	-113	28	-948	279	-168	84
-116.3378	34.6451	-35.2	283	113	-156	28	-999	266	-147	82
-116.3313	34.6374	-36.2	226	113	-269	28	-1100	259	-62	81
-116.3256	34.6314	-38.8	170	85	-594	28	-1600	187	111	60
-116.3190	34.6248	-39.8	141	28	-735	57	-1799	130	191	30
-116.3124	34.6183	-38.8	28	28	-905	57	-1957	133	331	30
-116.3058	34.6113	-41.0	-113	57	-1103	71	-1982	181	518	48
-116.2988	34.6054	-43.1	-184	113	-1244	85	-2040	272	633	84
-116.2922	34.5993	-40.8	-226	141	-1301	113	-2160	364	673	107
-116.2854	34.5926	-37.4	-311	141	-1357	141	-2261	432	735	113
-116.2785	34.5845	-33.6	-283	141	-1301	113	-2419	430	668	111
-116.2729	34.5771	-28.8	-198	85	-1216	85	-2777	327	536	71
-116.2673	34.5678	-21.5	-113	57	-1103	85	-3551	366	345	52
-116.2641	34.5586	-16.7	-85	57	-905	57	-3741	365	196	55
-116.2604	34.5489	-14.2	-85	57	-679	57	-3177	428	121	59
-116.2580	34.5390	-10.6	-57	42	-537	57	-3440	506	-0	52
-116.2561	34.5298	-8.9	0	42	-481	57	-4076	599	-123	59
-116.2546	34.5208	-8.7	57	42	-452	57	-4410	613	-201	60
-116.2527	34.5112	-9.5	141	42	-339	57	-3807	560	-251	56
-116.2508	34.5021	-11.1	170	57	-283	57	-3098	548	-229	67
-116.2484	34.4931	-16.8	198	57	-339	57	-2443	364	-146	55
-116.2447	34.4854	-19.4	212	57	-396	42	-2403	279	-117	51
-116.2417	34.4774	-20.9	226	57	-481	28	-2604	233	-94	50
-116.2374	34.4698	-27.5	226	57	-537	42	-2170	201	-15	46
-116.2317	34.4616	-29.2	240	57	-537	42	-2093	190	-13	45
-116.2261	34.4531	-32.4	255	57	-594	28	-2081	155	17	43
-116.2197	34.4460	-41.1	269	57	-622	42	-1781	141	64	42
-116.2117	34.4395	-46.4	283	57	-622	57	-1641	145	76	44
-116.2044	34.4340	-49.1	255	57	-566	42	-1425	123	80	41
-116.1963	34.4285	-52.0	240	57	-537	42	-1297	118	85	41
-116.1884	34.4237	-53.8	212	57	-537	28	-1220	103	108	38
-116.1804	34.4189	-49.9	198	42	-566	42	-1310	103	119	33
-116.1740	34.4137	-46.2	198	42	-594	57	-1442	129	120	37
-116.1656	34.4072	-45.3	198	42	-566	42	-1412	111	105	33
-116.1579	34.4006	-44.7	184	42	-523	42	-1320	112	95	33

-116.1504	34.3945	-45.3	170	42	-523	42	-1281	111	106	33
-116.1432	34.3886	-40.6	156	42	-509	28	-1341	103	95	31
-116.1362	34.3809	-32.4	141	42	-509	28	-1594	125	71	33
-116.1304	34.3719	-28.2	141	42	-396	28	-1495	142	12	34
-116.1252	34.3639	-27.2	127	42	-368	28	-1420	146	10	34
-116.1199	34.3551	-26.1	113	42	-311	28	-1267	152	-1	35
-116.1154	34.3475	-24.7	113	42	-283	28	-1243	160	-16	35
-116.1101	34.3376	-24.3	99	42	-170	28	-857	163	-36	36
-116.1059	34.3301	-24.0	85	42	-113	28	-640	165	-40	36
-116.1020	34.3226	-24.1	85	42	-57	28	-454	164	-55	36
-116.0977	34.3150	-29.4	71	42	-57	28	-341	136	-36	34
-116.0915	34.3073	-33.1	57	28	-57	28	-272	96	-22	23
-116.0863	34.3006	-36.7	42	28	-57	28	-218	88	-9	23

angle in degrees, distance in millimeters

Table 2. Surface Slip - western strand

			ascending		descending		strike		dip	
longitude	latitude	azi.	los	σ	los	σ	slip	σ	slip	σ
-116.3764	34.7191	-19.3	-57	28	113	28	676	159	30	26
-116.3733	34.7098	-15.0	-141	42	113	28	1288	258	134	43
-116.3704	34.7008	-12.1	0	85	226	28	1416	560	9	96
-116.3686	34.6920	-10.0	0	57	283	28	2139	478	48	71
-116.3665	34.6826	-13.0	-85	57	339	28	2475	369	92	61
-116.3635	34.6736	-17.7	-113	57	396	28	2197	273	46	53
-116.3595	34.6645	-21.6	-113	57	452	42	2022	253	-5	50
-116.3551	34.6560	-25.2	-198	42	481	42	2097	185	28	36
-116.3496	34.6472	-28.4	-339	42	509	28	2345	141	105	34
-116.3440	34.6392	-32.1	-424	42	566	14	2446	111	121	32
-116.3380	34.6319	-35.3	-311	42	679	28	2247	116	-25	32
-116.3320	34.6252	-36.0	-226	28	877	57	2463	141	-163	29
-116.3259	34.6182	-37.3	-170	42	933	57	2390	153	-233	37
-116.3192	34.6114	-37.7	-198	57	905	57	2366	172	-205	45
-116.3128	34.6042	-38.6	-198	57	820	57	2143	168	-178	45
-116.3060	34.5977	-41.3	-141	42	735	57	1743	141	-198	37
-116.2995	34.5918	-40.4	-113	42	707	57	1663	143	-202	37
-116.2928	34.5849	-39.8	-57	57	764	57	1682	164	-261	45
-116.2857	34.5781	-37.9	57	57	735	57	1451	171	-321	45
-116.2802	34.5716	-32.9	113	62	679	57	1368	203	-320	50
-116.2745	34.5639	-25.1	198	71	650	42	1403	256	-339	59
-116.2711	34.5556	-18.2	283	71	594	42	1308	347	-358	66
-116.2677	34.5468	-12.9	339	71	566	42	1335	487	-367	77
-116.2661	34.5374	-6.3	396	99	537	28	1680	1223	-347	166
-116.2652	34.5279	-4.3	368	85	481	28	1998	1579	-271	191
-116.2644	34.5188	-5.6	339	71	438	28	1342	1033	-295	131
-116.2630	34.5093	-8.3	283	57	368	28	769	573	-281	80
-116.2611	34.5000	-10.4	85	57	283	28	1439	460	-65	69
-116.2586	34.4899	-14.2	0	57	184	42	984	379	-9	59
-116.2552	34.4809	-22.9	57	42	170	28	381	172	-89	36
-116.2498	34.4727	-29.6	0	42	198	28	526	136	-64	34
-116.2446	34.4655	-30.0	-141	42	113	42	668	157	71	35
-116.2388	34.4570	-30.2	-170	42	170	42	887	157	73	35

-116.2329	34.4490	-25.6	-113	42	226	42	1033	183	28	36
-116.2288	34.4398	-12.6	-57	42	226	28	1709	308	67	47
-116.2273	34.4282	-7.7	-28	42	198	28	2220	500	118	63
-116.2252	34.4176	-14.8	-28	57	170	28	1018	325	17	58
-116.2206	34.4071	-26.0	-28	57	141	28	509	190	-18	46
-116.2143	34.3992	-34.1	0	57	113	28	265	148	-40	42
-116.2079	34.3917	-37.8	0	28	113	28	242	86	-43	23
-116.2011	34.3852	-40.5	0	28	113	28	229	81	-45	23
-116.1945	34.3787	-39.3	28	28	85	28	117	83	-53	23
-116.1877	34.3717	-37.3	14	28	71	28	123	87	-37	23
-116.1820	34.3652	-36.9	0	28	57	28	124	87	-21	23
-116.1759	34.3587	-37.7	0	28	42	28	91	86	-16	23
-116.1695	34.3519	-34.2	-14	28	28	28	99	93	0	23
-116.1646	34.3450	-29.0	-28	42	20	28	130	138	15	34
-116.1599	34.3376	-27.6	-14	28	14	28	80	113	7	24
-116.1555	34.3307	-27.4	0	28	8	28	24	114	-3	24
-116.1504	34.3226	-25.4	14	28	6	28	-26	122	-13	24
-116.1455	34.3134	-26.4	28	28	0	28	-84	118	-23	24
-116.1403	34.3058	-30.4	28	28	-6	28	-88	104	-20	23
-116.1341	34.2974	-32.7	28	28	-14	28	-103	97	-16	23
-116.1274	34.2892	-38.5	57	28	-28	28	-179	84	-29	23
-116.1187	34.2814	-42.5	57	28	-28	28	-165	78	-27	22
-116.1112	34.2746	-42.4	57	28	-57	28	-220	78	-16	22

angle in degrees, distance in millimeters